Multiferroic $BaCoF_4$ in thin film form: ferroelectricity, magnetic ordering, and strain

Pavel Borisov,[†] Trent A. Johnson,[†] Andrés Camilo García-Castro,[‡] Amit KC,[†] Dustin Schrecongost,[†] Cheng Cen,[†] Aldo H. Romero,[†] and David Lederman[*,†,¶]

[†]*Department of Physics and Astronomy, West Virginia University, Morgantown WV 26506-6315, USA*

[‡]*Physique Théorique des Matériaux, Université de Liège, B-4000 Sart-Tilman, Belgium*

[¶]*Department of Physics, University of California, Santa Cruz, CA 95064, USA*

E-mail: david.lederman@mail.wvu.edu

Abstract

Multiferroic materials have simultaneous magnetic and ferroelectric long-range orders and can be potentially useful for a wide range of applications. Conventional ferroelectricity in oxide perovskites favors non-magnetic electronic configurations of transition metal ions, thus limiting the number of intrinsic multiferroic materials. On the other hand, this is not necessarily true for multiferroic fluorides. Using molecular beam epitaxy, we demonstrate for the first time that the multiferroic orthorhombic fluoride $BaCoF_4$ can be synthesized in thin film form. Ferroelectric hysteresis measurements and piezoresponse force microscopy show that the films are indeed ferroelectric. From structural information, magnetic measurements, and first principles calculations, a modified magnetic ground state is identified which can be represented as a combination of bulk collinear antiferromagnetism with two additional canted spin orders oriented along orthogonal axes of the $BaCoF_4$ unit cell. The calculations indicate that an anisotropic epitaxial strain is responsible for this unusual magnetic ground state.

Keywords

Multiferroics, thin films, fluorides, ferroelectricity, antiferromagnetism

1 Introduction

Multiferroic materials exhibit exciting physical phenomena related to the simultaneous presence of multiple long-range orders, in many cases consisting of antiferromagnetism and ferroelectricity. To date, the majority of studies on multiferroic materials have been devoted to oxide perovskites in the form ABO_3. The conventional ion transfer ferroelectricity mechanism in oxide perovskites is known to rely on the covalent bonds between oxygen and B-site cations with closed-shell, non-magnetic electronic configurations.[1,2] Therefore, the search for magnetic ferroelectrics should be directed towards alternative ferroelectricity mechanisms. Alternatives can be found in the fluoride family which contains many examples of magnetic ferroelectrics.[3] The best known example is the $BaMF_4$ compound, where M=Mn, Fe, Co, or Ni. Recent theoretical studies[4,5] focused on their magnetoelectric and multiferroic properties. To the best of our knowledge, however, only studies of bulk form $BaMF_4$ have been reported in the scientific literature.[3,6–15] Because thin films are essential for potential electronic device implementations, including heterostructure integration with existing architectures, it is important to determine whether these materials can be synthesized in thin film form, and whether the multiferroicity can be retained if growth strain is applied.

$BaMF_4$ compounds crystallize in orthorhombic lattice with the space group $Cmc2_1$.[16] Distorted MF_6 octahedra share corners in the *ac*-plane, forming puckered sheets which are separated by Ba ions along the *b*-axis (Figure 1a).[5] Their long range ferroelectric (FE) order theoretically originates from MF_6 octahedra rotations about the *a*-axis and polar displacements of Ba cations along the *c*-axis.[5] The combination of these two effects results in geometric proper ferroelectricity. The FE switching barrier is expected to be of the same order of magnitude for the whole family of M=Mn, Co, Fe, Ni. Previous experiments in bulk single

crystals demonstrated FE switching with c-axis saturation polarizations of $P_S = 8.0$ μC/cm^2 and 6.7 μC/cm^2 and FE Curie temperatures of 1153 K and 1593 K in $BaCoF_4$ and $BaNiF_4$, respectively, but no switching in $BaFeF_4$ and $BaMnF_4$.[6,10] The lack of FE switching in $BaFeF_4$ was explained by the increased conductivity of crystalline samples. However, the theoretical analysis of Ederer and Spaldin has suggested that FE switching in the Mn and Fe compounds may require electric fields larger than those applied in the experiments.[5] Note that a similar crystal structure and geometrical (or topological) ferroelectricity have recently been studied in the orthorhombic oxide polymorph $LaTaO_4$,[17] and therefore our results can be relevant to this broader class of materials.

Since the inter-planar spacing along the b-axis ($\approx$ 15 Å) is much larger than the intra-planar lattice constant ($\approx$ 4 Å), the antiferromagnetism in $BaMF_4$ has a pronounced two-dimensional character. With nearly linear M-F-M-F chains along the a-axis, and zigzag M-F-M-F configurations along the c-axis (e.g., the Co-F-Co bonding angle is 146.5° in $BaCoF_4$),[7,11] antiferromagnetic (AF) interactions between M^{2+} magnetic moments are strongest in the ac-plane. Spins in $BaMF_4$ are oriented along the b-axis, except in $BaCoF_4$, where they point along the c-axis ($c = 5.85$ Å).[8]

For $BaCoF_4$, the bulk magnetic order consists of a collinear antiferromagnet with a Néel temperature of $T_N = 69.6$ K. Broad maxima in the magnetic susceptibility at $T = 110$ K and 90 K are observed with the external magnetic field H applied parallel and perpendicular to the c-axis, respectively.[11] The bulk spin order consists of two simultaneously present distinct phases, A and B, both of which order in three dimensions at the same T_N. Phases A and B result from negative and positive signs of the inter-planar magnetic exchange coupling along the b-axis (see Supporting Information, Figure S5). Phases A and B were found to appear in a 9 : 11 ratio in the single crystal.[11] The magnetic phase A of $BaCoF_4$ has the magnetic monoclinic space group P_a2_1;[5,11,18] an alternative description within the orthorhombic basis consists of the orthorhombic crystal unit cell doubled along a- and c-axes.[11] Phase B of $BaCoF_4$ corresponds to the orthorhombic magnetic space group P_bca2_1,[11,18] with the

orthorhombic crystal unit cell doubled along the a-axis only. The corresponding magnetic point groups are $21'$ and $mm21'$, respectively, and thus weak ferromagnetic (WFM) order is forbidden in both cases.

A linear magnetoelectric (ME) effect was reported in $BaCoF_4$[19,20] in 1970, however, later studies[11] found that this effect contradicts the magnetic symmetry group in $BaCoF_4$. In addition, the original finding[19] of spontaneous magnetic moment was not confirmed for single crystals of $BaCoF_4$.[11] In the related compound $BaMnF_4$, the dielectric constant along the polar c-axis was found to decrease below $T_N = 29$ K. This effect disappeared in $BaMn_{0.99}Co_{0.01}F_4$, a compound which is known to reverse the spin easy axis from the b-axis to the c-axis, that is, to the $BaCoF_4$-case, and to remove the spin canting observed in $BaMnF_4$.[21] The ME effect observed in $BaMnF_4$ was explained by the existence of a non-linear term of the type $\boldsymbol{P} \cdot (\boldsymbol{L} \times \boldsymbol{M})$ in the free energy, where $\boldsymbol{P}$, $\boldsymbol{L}$ and $\boldsymbol{M}$ are vectors corresponding to the FE polarization, AF sublattice magnetization, and weak uncompensated magnetization due to the spin canting, respectively.[21–24] This mechanism is similar[25] to the one recently proposed to be responsible for hybrid improper ferroelectricity in $Ca_3Mn_2O_7$, where a trilinear coupling between the polarization $\boldsymbol{P}$ and two non-polar octahedral distortion modes of different symmetry, Q_1 and Q_2, takes place, while the distortion modes are additionally responsible for the linear ME effect and weak ferromagnetism, respectively.[26]

2 Experimental and Computational Methods

2.1 Thin film growth

Single-side polished Al_2O_3 (0001) substrates (MTI Corp. USA) were cleaned and then annealed in a tube furnace oven at 1200 °C for 2 hours in air in order to clean and reconstruct the surface. Once loaded into the MBE growth chamber, all substrates were annealed in vacuum at 700 °C for one hour before reducing the temperature to the desired growth temperature. Films of $BaCoF_4$ were deposited by co-deposition of BaF_2 and the appropriate

transition metal fluoride, CoF_2, using commercial Knudsen cells. Prior to the growth, the deposition rates of each material were measured by a quartz crystal monitor placed at the position of the substrate holder, and then the rates were adjusted to achieve the proper stoichiometry. Typical growth rates for BaF_2 were 0.005 nm/s, while the growth rates for CoF_2 were adjusted accordingly to achieve a 1 : 1 molar ratio between both constituents. Typical growth rates were 0.006-0.007 nm/s for $BaCoF_4$. Several sets of substrate temperatures, $T_S = 300 - 500$ °C, were tested in order to optimize the structural quality of the samples. The best growth, as judged from the x-ray diffraction measurements, was achieved at $T_S = 350 - 400$ °C. The total thickness of $BaCoF_4$ films was adjusted to 100 nm.

Pt interdigitated electrodes were deposited on Al_2O_3 substrates prior to the growth of $BaCoF_4$ thin film samples later used later for FE measurements. Pt was deposited by DC magnetron sputtering at room temperature at growth rates of 0.033 nm/s to the total film thickness of 50 nm. Standard ultraviolet optical photolithography procedures were used to create the photoresist mask for interdigitated electrodes. The electrodes consisted of 25 pairs of fingers separated by a 2.5 μm gap, with a finger length of 0.5 mm and a width of 5 μm.

2.2 Structural characterization

Structural characterization of the thin films was performed by x-ray diffraction using a Rigaku Cu rotating anode source, a Huber four-circle goniometer, and a bent crystal graphite monochromator tuned to the Cu K_α radiation (0.15418 nm wavelength).

2.3 Magnetic measurements

Magnetization measurements were performed using a Magnetic Properties Measurement System (MPMS) based on a Superconducting Quantum Interference Device (SQUID) sensor from Quantum Design. All measurements were corrected by subtracting the magnetic response from a blank, diamagnetic Al_2O_3 substrate.

2.4 Ferroelectric hysteresis loops

In-plane FE polarization of the thin films samples was measured using Pt interdigitated electrodes deposited on top of the substrate and covered by the film during its growth. FE hysteresis measurements were performed using a Precision LC tester from Radiant Technologies. Each hysteresis loop was averaged 250 times. Thin film samples were mounted in a closed-cycle helium cryostat from CryoMech and cooled to a base temperature of approximately 14 K. Electrical contacts between tester wires and the interdigitated electrodes were made with indium.

In order to remove the effects of the relatively large parallel capacitance associated with the wires running through the cryostat, as well as of current leakage effects, the remanent hysteresis option was used as implemented into the Radiant tester software. This approach is essentially an extension of the PUND (Positive Up Negative Down) method but applied to the hysteresis measurements. A pre-set unipolar triangular voltage pulse was applied prior to each bipolar triangular voltage pulse used for the actual polarization measurement. Depending on the field direction of the preset pulse with respect to the field direction during the first half of the subsequent measurement pulse, the corresponding loop is then labeled as unswitched or switched. Switched and unswitched loops were performed for both positive and negative initial field directions. The difference between switched and unswitched loops was used to extract the contribution to the overall signal that is due to FE behavior.

To test the reliability of this procedure, a remanent hysteresis of a definitively non-FE sample, BaF_2 film grown on Al_2O_3 substrate using identical interdigitated electrodes, was performed and no response was detected.

2.5 Piezoresponse force microscopy

PFM measurements were performed at room temperature using Asylum Research MFP-3D AFM system. Platinum-coated silicon cantilevers (Olympus OMCL-AC240TM) were used in the measurements. PFM amplitude and phase were measured at the contact resonance

frequencies of the probes, typically around 360 kHz.

2.6 First-principles calculations

First-principles calculations were performed within Density Functional Theory (DFT) as implemented in the Vienna Ab initio Simulation Package (VASP).[27,28] Projector augmented wave (PAW) pseudo-potentials[29] were used to represent the valence and core electrons. The electronic configurations taken into account in pseudo-potential as valence electrons were Ba ($5s^2 5p^6 6s^2$), Co ($3p^6 3d^7 4s^2$) and F ($2s^2 2p^5$). The exchange correlation was represented within the General Gradient Approximation (GGA) and Perdew-Burke-Ernzerhof for Solids (PBEsol) parameterization.[30] Due to the magnetic character of these systems, the spin polarization was considered in the calculation with the proper use of an exchange correlation functional (LSDA). The periodic solution of these crystalline structures was represented by Bloch states with a Monkhorst-Pack with a $4\times4\times6$ k-point mesh and a 600 eV energy cut-off, which has been previously demonstrated to give converged forces to less than 0.0001 eV/Å. Additionally, the correct description of the d-electron localization was achieved through the DFT+U approximation with $U = 4.0$ eV.[31] Spin-orbit coupling (SOC) in the non-collinear analysis was included according to the implementation by Hobbs et al.[32] In order to take into account the AF magnetic interactions along the a-axis, a $2 \times 1 \times 1$ (48 atoms) cell was used for all the calculations. Finally, the spontaneous polarization was computed within the Berry phase approach as implemented in VASP.[33–35]

3 Results and Discussion

3.1 Material parameters and substrate considerations

The choice of substrates suitable on which to grow $BaMF_4$ films is non-trivial because the orthorhombic unit cell makes it difficult to find a substrate with good in-plane lattice match. For reference, the lattice parameters for M=Co are $a = 4.21$ Å, $b = 14.63$ Å, and $c =$

5.85 Å.[7] In our experiments, Al_2O_3 (0001) single crystalline substrates (hexagonal unit cell a = 4.763 Å; c = 12.991 Å) were used. As shown in Figure 1b, four (010) unit cells of $BaCoF_4$ can fit along the [001] direction, consisting of five (0001) unit cells of Al_2O_3 along $[11\bar{2}0]$, which results in theoretical lattice mismatches along the a-axis of 2.0% (compressive strain) and -1.8% (tensile strain) along the c-axis.

3.2 Growth and structural characterization

Thin films were grown under ultra-high vacuum conditions using molecular beam epitaxy (MBE). Two constituents, BaF_2 and CoF_2, were co-evaporated in 1 : 1 molar rates.

The out-of-plane x-ray diffraction (XRD) scan on the best quality 100 nm $BaCoF_4$ film (Figure 2a) shows a predominant (010) orientation, with the secondary orientation peaks (170), (190) and $(1\underline{1}\underline{1}0)$ adjacent to (080), $(0\underline{1}\underline{0}0)$ and $(0\underline{1}\underline{2}0)$ peaks, respectively. That is, formation of stalking faults in the ab-plane causes a deviation from the preferential (010) orientation. In the projection onto the ab-plane, the unit cell contains four $BaCoF_4$ monolayers (Figure 1a). The (150) orientation was not observed, possibly because the angle between (150) and (060) planes is 35°, which is much larger than the angles of 26°, 21°, and 18° for the observed reflections from the (170), (190) and $(1\underline{1}\underline{1}0)$ planes, respectively. No additional impurity phases were observed. Additional tests provided no evidence for the formation of Ba_2CoF_6 and $Ba_2Co_3F_{10}$ impurity phases[7] (see Supporting Information).

Rocking curves measured at the (040) $BaCoF_4$ Bragg condition (Figure 2b) showed full-widths at half maximum (FWHM) of 0.58°. The corresponding rocking curve of the (0006) peak of Al_2O_3 substrates was FWHM= 0.25° (Figure 2b), which was limited by the instrumental resolution. Φ-scans around the $BaCoF_4$ (041) and Al_2O_3 $(10\bar{1}4)$ peaks are shown in Figure 2c. The symmetry of the peaks can be explained in both materials by the formation of three in-plane structural twin domains rotated by 120° with respect to each other. The polar c-axis in each of the twin domains grew along the Al_2O_3 substrate's three $\langle 11\bar{2}0\rangle$ directions, as shown in Figure 1b.

Based on the asymmetrical scans of the $BaCoF_4$ (041), (082), (111), (222) and (333) peaks, the unit cell parameters were calculated to be $a = 4.20 \pm 0.01$ Å, $b = 14.56 \pm 0.01$ Å, and $c = 5.93 \pm 0.01$ Å. These values are in agreement with the compressive and tensile strains imposed by the Al_2O_3 substrates, since the in-plane a-lattice parameter was reduced by 0.2% and the c lattice parameter increased by 1.4% with respect to the bulk values. The reduction of the a lattice constant was within the experimental error, however, and therefore cannot be completely proven. The in-plane lattice mismatch also led to a decrease of 0.5% for the out-of-plane lattice parameter b, also with respect to the bulk. In summary, the films were strained by the interaction with the substrate, mostly along the polar c-axis, with the parameter b adopting a new value. The unit cell volume of $BaCoF_4$ increased by $0.6 \pm 0.3\%$ with respect to the bulk.

3.3 Ferroelectric properties

3.3.1 Ferroelectric hysteresis loops

$BaMF_4$ compounds are expected to have FE polarizations along the crystallographic c-axis. In our case, this means that the electric field should be applied in the film plane. This was achieved by depositing interdigitated electrodes directly on the substrate surface prior to the film growth (see Supporting Information and Figure 3a). A separate sample without the electrodes was grown simultaneously in order to verify the film crystal quality by x-ray diffraction.

The electrodes were aligned such that the electric field direction applied during the measurements was perpendicular to the polar c-axis of one twin domain and at 30° with respect to the other two domains (Figure 3a). Therefore, assuming the three in-plane crystal orientations are equally weighted, the measured response should be $1/\sqrt{3}$, or approximately 58% of the single twin domain polarization. The leakage of the samples at room temperature was relatively high, and thus reliable FE hysteresis loops could not be measured. To minimize the leakage, FE measurements were performed at a temperature $T \approx 14$ K.

Remanent hysteresis loops were measured up to a maximum electric field of 3.95×10^7 V/m, as shown in Figure 3b. The remanent polarization of the largest loop was ≈ 1.1 μC/cm^2, which is of the same order of magnitude as the 8.0μC/cm^2 measured in the bulk,.[10] Actual hysteresis loops have never been published for bulk $BaCoF_4$, to the best of our knowledge. We therefore tentatively compare our loops with data reported for $BaZnF_4$.[36] Typical coercive fields for $BaZnF_4$ were reported to depend strongly on the ac field frequency, ranging from 1.0×10^6 to 6.0×10^6 V/m for ac field frequencies between 0.01 Hz and 100 Hz, respectively. Since our measurements were performed with 100 ms electric field pulse duration, corresponding to a 10 Hz field frequency, and therefore a 3.35×10^6 V/m coercive field would be expected if the compound were $BaZnF_4$. In our case, the measured coercive fields were $\approx 2.5 \times 10^7$ V/m. In order to compare the two results, the semi-empirical scaling law for the coercive field E_C vs. distance between contacts d, $E_C(d) \sim d^{-2/3}$, can be used.[37] Using the separation between contacts of 2.5 μm, a calculation reveals that $BaZnF_4$ should have $E_C = 1.41 \times 10^8$ V/m, or approximately six times larger than the value measured in our $BaCoF_4$ film. It is unclear whether this difference is due to an intrinsic property of the Co compound or if E_C was reduced by the presence of defects in the film.

Regarding the maximum remanent polarization measured in $BaCoF_4$, we note that, taking into account the presence of the three in-plane domains, the actual polarization should be 3 times the measured polarization, or ≈ 2 μC/cm^2. This is still lower than the value of 8.1 μC/cm^2 measured in the bulk material, but there are other factors that may have led to an underestimate, for example, there could be regions in the film that had larger switching fields than we were able to apply with our technique.

3.3.2 Piezoresponse force microscopy (PFM)

PFM[38–42] was performed at room temperature to characterize the microscopic polar domains and FE properties of the $BaCoF_4$ films. Typical topography image and PFM responses are shown in Figure 4a. A root-mean-squared (rms) surface roughness of 3.0 nm was observed

across the sample while the PFM responses revealed a granular sub 100 nm domain pattern. PFM data were acquired using the out-of-plane flexural vibrational mode of the cantilever. The in-plane torsional mode was also monitored but did not yield a significant signal, possibly due to the cantilever's high torsional rigidity. In the experiments, a small ac drive voltage of 1 V at the cantilever contact resonance frequency was applied to the buried electrodes array while the scanning probe was kept at the ground potential. Underneath the probe tip, a localized electric field (E_{tip}) was generated with both an out-of-plane field component and opposite in-plane components at opposing sides of the tip (Figure 4b). The surface deformation of the film with in-plane polar c-axes in response to E_{tip} is illustrated in Figures 4c and 4d. In the middle of a domain, the out-of-plane deformation was small and mainly coupled to the cantilever's flexural mode through a weak shearing force (Figure 4c). However, at the boundary between two domains with head-to-head polarizations, the in-plane gradient of E_{tip} induced a large out-of-plane deformation which strongly coupled to the cantilever's flexural vibration mode (Figure 4d). In the special case when the c-axis was perpendicular to the cantilever, the torsional shearing response was not detectable by flexural PFM.

The phase of the PFM signal induced by shearing force depended on the relative orientation between the local c-axis and the probe cantilever. In contrast, the PFM signal induced by out-of-plane deformations at domain boundaries was independent of such orientation changes. Therefore, information of the local c-axis orientations could be extracted by comparing the PFM phases after sample rotations (Figure 4e). Note that as expected, the overlaid PFM amplitude image in Figure 4e showed the strongest signals at domain boundaries. PFM results also supported the presence of three different c-axis orientations deduced from XRD measurements. Figure 4f shows the histograms of the phase differences $\Delta\phi$ measured after rotating the sample by 180° in two orthogonal configurations. The values of $\Delta\phi$ were concentrated mostly around 0 and $\pm\pi$. Values around $\Delta\phi = 0$ corresponded to domain boundaries and domains with polar c-axes perpendicular to the cantilever, while values around $\Delta\phi = \pm\pi$ corresponded to domains with nonzero polarization components

along the cantilever orientations. As expected, in the configurations when the cantilever was perpendicular to one of the c-axis orientations indicated by XRD (colored red in Figure 4f), the distribution at $\Delta\phi = 0$ increased significantly.

To evaluate the FE properties of the nano-domain structures, an in-plane electric field was applied by biasing the interdigital electrodes. Restricted by leakage, dc electric fields (E) between -3.1×10^7 V/m and 4.2×10^7 V/m were applied. Figure 5a shows the PFM images taken in a 175 nm $\times$ 175 nm area after different values of E were applied during 30 s and then turned off. During the measurements, the cantilever was aligned parallel to the dc field orientation. A π-phase shift was observed only in some regions (e.g. regions highlighted by yellow dash curves) during the field sweep. It is likely that the regions that did not switch contained twin domains with their polar axes largely perpendicular to E and other regions that required higher electric field to switch.

Head-to-head domain boundaries were identified from regions with large PFM amplitudes and opposite phases at opposing sides, as discussed above. PFM amplitudes at such locations were tracked as a function of E. In principle, because large electric fields aligned the polarizations of adjacent domains, the PFM amplitude was expected to be minimized at both field polarities as illustrated in Figure 5b. However, when one domain required a switching field larger than what was possible in the experiments, the PFM amplitude evolution was expected to be different (Figure 5c). In the experiment two separate spots were studied. One spot (left, Figure 5d) was located between the electrodes, while the other one, as a control experiment, was located on top of a buried electrode (right, Figure 5d) where the in-plane field was zero. Large hysteretic changes of PFM amplitude were only observed in the first case and resembled the situation of a limited domain switching, as illustrated in Figure 5c. The fact that some domains required much larger switching field than others might originate from a preferred polarization direction in the film or other reasons related to leakage.

3.4 Magnetic properties

Zero-field cooling (ZFC), field cooling (FC), and thermoremanent magnetizations (TRM) were measured as a function of temperature by heating in a magnetic field applied after cooling in zero-field, during cooling in non-zero field and upon heating in zero-field after a FC procedure, respectively. Figure 6a shows magnetization M vs. T data for a $BaCoF_4$ thin film. A broad maximum was observed at approximately 80 K, which is relatively close to the expected maxima which occur at 90-110 K in the bulk. There was no splitting between the ZFC and FC curves at the 80 K maximum down to approximately 50 K (inset in Figure 6a), indicating that this transition corresponds to collinear AF bulk-like spin order. The low temperature magnetic response shows two additional transitions at $T_{C1} = 19$ K and $T_{C2} = 41$ K, which are not observed in bulk $BaCoF_4$. Both transitions appear to correspond to weak ferromagnetic (WFM) order because of the relatively low magnetization values and the shape of the hysteresis loops, as discussed below. Qualitatively, the new magnetic transitions can be explained by the strain in the films. The largest strain was along the c-axis, which is also the direction of the AF vector L_c for collinear order $L_c = s_1 - s_2 - s_3 + s_4$, where s_1, s_2, s_3, and s_4 are spin moments at different Co sites labeled in Figure 1c. Therefore a more pronounced modulation of the bulk spin order by the strain is expected. The two transitions were also visible in the TRM (Figure 6b). Surprisingly, the remanent magnetization could be prepared by cooling in magnetic fields aligned both in the film's plane and out of the film's plane. These results are consistent with the first-principles calculations, discussed in more detail below, which show that two additional magnetic spin cantings, along the b- (out of the film plane) and a- (in the film plane) axes, are energetically favorable when strain is taken into account. In particular, the additional canted AF order as allowed in $BaCoF_4$ along the b-axis, is then again similar to analogous AF canted order L_c along the c-axis theoretically predicted for $BaNiF_4$.[4]

Additional information about the magnetic transitions in $BaCoF_4$ was provided by magnetic hysteresis loops measurements shown in Figure 6c. Hysteresis loops measured at

$T = 5$ K had a shape similar to other weak ferromagnetic materials, such as $YFeO_3$.[43] The remanent magnetization was approximately 0.05 μ_B per formula unit, which agrees well with typical values for weak ferromagnetism and is in agreement with the theoretical value of 0.03 μ_B per formula unit derived from our *ab-initio* calculations discussed below. Magnetic fields up to 30 kOe were necessary to saturate the loop at $T = 5$ K. This feature is also typical for weak ferromagnetic thin film materials and can be explained by the existence of domains with the spin canting magnetization parallel (low saturation fields) and perpendicular (high saturation fields) to the applied magnetic field direction. These domains are due to the structural domains rotated by 120° with respect to each other present in our samples. Magnetic hysteresis loops measured at temperatures $T > 20$ K showed mostly a linear response with closed loops. An s-shaped response at low fields, that was persistent up to room temperature was also observed, can be explained by superparamagnetic impurities in Al_2O_3 substrates, as verified by measurements on blank substrates.

3.5 First principles calculations

Spontaneous polarization and non-collinear magnetism in $BaCoF_4$ thin films were calculated using density functional theory assuming epitaxial strain and structural lattice parameters similar to the experimental values obtained from thin films grown on Al_2O_3 (0001) substrates. The thermal stability of the strained $BaCoF_4$ phase was tested via phonon dispersion calculations using the lattice parameters obtained from XRD scans (+1.2% along the a-axis and +0.5% along the c-axis with respect to the theoretically optimized bulk cell parameters, $a_0 = 4.1556$ Å, $b_0 = 14.4981$ Å, and $c_0 = 5.9034$ Å). No imaginary frequencies (unstable modes) were found, indicating that that the bulk space group $Cmc2_1$ for this strain value was stable without additional structural transitions.

In order to determine the impact of the strain on the FE properties, the polarization change was calculated as a function of strain applied isotropically along the ac-plane (Figure 7a). In addition, the magnetic spin structure with the lowest energy was evaluated for

specific isotropic strain values of -4%, 0%, 4%, as well as for the experimental a- and c-lattice parameters (Table 1). Note that the experimental strain was consistent with our experimental results and anisotropic.

Table 1: Magnetic moment per formula unit (or Co atom) along each axis (a, b, and c) for each magnetic ordering where the G_c is the main collinear AF order and C_b and F_a are the WAF and WFM spin orders, respectively. All strains are isotropic in the ac plane, except for the 1.2% strain result which was calculated with strain applied only along the c-axis, per experimental results.

	Magnetic Moments (μ_B/formula unit)		
Strain	G_c	C_b	F_a
-4%	2.775	0.107, 0.069	0.000
0	2.762	0.130, 0.044	0.038
+1.2% (exp.)	2.766	0.124, 0.051	0.039
+4%	2.789	0.103, 0.080	0.000

Figure 7a shows the calculated spontaneous polarization as a function of the isotropic ac-plane elastic strain. For tensile or compressive strain values of -4% and +4%, the polarization increased by 0.6 μC/cm^2 and 1.2 μC/cm^2, respectively, relative to the unstressed bulk state. A non-linear, non-monotonic coupling of the polarization to the strain was found, with a minimum near zero-strain, suggesting a non-linear second order piezoelectric response to the applied strain. This behavior is the opposite of what is usually observed in oxide perovskites, where a linear dependence of the polarization as a function of the bi-axial strain has been calculated,[44] but is similar to the second order piezoelectric effect found in semiconductors with the zincblende structure.[45] The polarization developed along the crystallographic c-axis, in agreement with bulk behavior.[11] 11 For a value of the isotropic epitaxial strain corresponding to the strain along the in-plane c-axis (1.2%), a polarization value $P_s = 10.1$ μC/cm^2 was calculated, while in the case of the experimental anisotropic strain, the polarization gives $P_s = 16.8$ μC/cm^2 (not shown in Figure 7a). This demonstrates the sensitivity of the FE polarization to the direction and sign of the strain. Figure 7b shows that the b-lattice parameter decreases as a and c increase, as expected from Poisson's ratio. Note that in the experiments a slight decrease of the lattice parameter a was found, which

indicates that the in-plane strain was actually anisotropic.

The bulk crystal structure of $BaCoF_4$ contains CoF_6 octahedra zig-zag chains along the c-axis (the Co-F-Co bonding angle is $\gamma = 146.5°$) and nearly linear Co-F-Co chains along the a-axis ($\gamma = 173.7°$), with $BaCoF_4$ puckered sheets stacked along the b-axis (Figure 1a). Figure 7c shows the modulation $\Delta\gamma$ of the calculated Co-F-Co bonding angle along a-axis as a function of the isotropic strain. As discussed below, this bonding angle modulation should affect the magnetic spin structure.

Non-collinear magnetism was studied assuming B-phase AF ordering as the magnetic structure in $BaCoF_4$, however the following results should apply to both A and B phases (see Supporting Information).

A secondary AF ordering along the b-axis in the form of canted spins [weak antiferromagnetic (WAF) order] (Figure 1c, middle) is allowed within the theoretical ground state, in addition to the main collinear AF order along the c-axis. Similar findings have been reported by Ederer and Spaldin for $BaNiF_4$.[4] By denoting the WAF and collinear magnetic orders as C_b and G_c, respectively, we found that G_cC_b is the ground state in the bulk $BaCoF_4$ (Figure 1c, middle). Note that the absolute magnitude of the canted (WAF) moment projection onto the b-axis alternates between two values, when followed along the c-axis. For the strain in our experiments, we calculated the canted moments to be 0.051 and 0.124 mu_B per formula unit (Table 1). This is explained by different octahedral tilts about the a-axis in adjacent corner-sharing CoF_6 octahedra with respect to the ac-planes. Using the strain value of our samples, the calculated corresponding angles were 24.0° and 57.1°. Magnetic moments associated with different spin orderings and strain values are listed in Table 1.

Our results are in good agreement with the previously reported calculated spin structure of $BaNiF_4$, where a Dzyaloshinskii-Moriya (DM) interaction was shown to induce WAF canting along the c-axis in addition to the bulk collinear AF spin order along the b-axis. By choosing same magnetic sites (Figure 1c, left) as for the case of $BaNiF_4$,[4] we obtain for the case of $BaCoF_4$ the AF vectors $L_c = s_1 - s_2 - s_3 + s_4$ and $L_b = s_1 + s_2 - s_3 - s_4$ for the

main AF collinear G_c and WAF G_b orders, respectively. These expressions are identical to the ones proposed for $BaNiF_4$ if $L_c(BaCoF_4)$ is replaced by $L_{ab}(BaNiF_4)$ and $L_b(BaCoF_4)$ is replaced by $L_c(BaNiF_4)$. That is, the magnetic structure obtained for $BaCoF_4$ was similar to the one proposed for $BaNiF_4$ but with the main AF order oriented along the c-axis and the WAF moment along the b-axis. Also, the absolute values of the WAF moments ($\approx 0.1\ \mu_B$ per formula unit) predicted for $BaCoF_4$ in this work and for $BaNiF_4$ are similar.[4] These analogies indicate that a DM interaction is present in both compounds.

For the anisotropic strain of 1.2%, corresponding to our experimental conditions, an additional WFM spin canting F_a along the crystal a-axis became energetically favorable, as explained below. Thus, the theoretical calculations predict that a WFM order is possible at low temperatures, in agreement with the experimental results that showed WFM behavior below $T_{C1} = 19$ K. Surprisingly, the calculated magnetic canted moment value, m_a, remained almost constant as a function of strain (Table 1). This can be explained by the competition between the DM interaction and the single-ion anisotropy, which is similar to that found in $CaRhO_3$.[46] In addition, the increased distortion of CoF_6 octahedra can result in non-zero off-diagonal components in the DM tensor, thus modifying the non-collinear ordering.

The thermal stability of the three aforementioned spin structures was also tested. To summarize the discussion so far, these structures consisted of a main G-type collinear AF order along the c-axis (G_c), a WAF canting along the b-axis as a first "slave" ordering (C_b), and a WFM canting as a second "slave" ordering along the a-axis (F_a). Initially, the total energy for the collinear AF spin order was calculated for the ground state G_c, and then the energy difference of the remaining two spin configurations with additional WAF (C_b) and WFM (F_a) orders was determined. The results are presented in Table 2. For the particular case of the anisotropic strain in our thin films, we found that the energy increased in the sequence $G_cC_bF_a \Rightarrow G_cC_b$ ($\Delta E = 19.21$ meV/formula unit) and $G_cC_b \Rightarrow G_c$ ($\Delta E = 17.67$ meV/formula unit). These results can explain the magnetic transitions observed in the $BaCoF_4$ experimental M vs. T data (Figure 6a and b). As T increases, a

gradual transformation from the ground $G_cC_bF_a$ state to G_c occurs as the available thermal energy overcomes the energy barriers. In comparison to unstrained (0% in Table 2) or strongly isotropically strained $BaCoF_4$ (+4% and -4% in Table 2), the corresponding energy difference between spin configurations without and with WFM ordering is much smaller in magnitude, ranging from 0.006 to 0.1 meV/formula unit. On the other hand, the WFM configuration is energetically unfavorable for +4% or -4% strain and only slightly favorable (by 0.01 meV/formula unit) for the relaxed theoretical cell. Therefore, the anisotropic strain along the c-axis causes the transition between the G_cC_b and $G_cC_bF_a$ states.

Table 2: Total energy per formula unit (or Co atom) calculated for each combination of magnetic spin orderings, G_cC_b and $G_cC_bF_a$, and energy difference between them for different values of the strain. All strains are isotropic in the ac-plane, except for the 1.2% strain result which was calculated with strain applied only along the c-axis, per experimental results. The large difference for the experimental strain value is likely due to the anisotropic strain.

	E_t (eV/formula unit)		
Strain	$E(G_cC_b)$	$E(G_cC_bF_a)$	ΔE
-4%	-5.5746	-5.5746	-0.006×10^{-3}
0	-5.5988	-5.5988	0.010×10^{-3}
+1.2% (exp.)	-5.5786	-5.5978	19.205×10^{-3}
+4%	-5.5627	-5.5627	-0.079×10^{-3}

In order to determine whether the hypothesis of three subsequent magnetic phase transitions is viable, further experimental TRM curves were measured (Figure 8). In order to make the lowest temperature WFM spin phase ($G_cC_bF_a$) visible in the experiments, the sample was cooled in a 1 kOe field applied only for $T < T_{C1} = 19$ K after zero- field cooling to T_{C1}. The corresponding TRM curve (Figure 8, red circles) shows a magnetization decrease at T_{C1}. Since the magnetic phase above T_{C1} was cooled in zero-field, and the coercive field for the G_cC_b phase was larger than 1 kOe for $T < T_{C1}$, the corresponding WAF spin order phase (G_cC_b) at $T_{C1} < T < T_{C2}$ was not magnetized. In order to magnetize only the WAF phase (G_cC_b) below $T_{C2} = 41$ K, 1 kOe was applied while cooling down to 23 K, and then the field was turned off while cooling down further to 5 K. The corresponding curve (Figure 8, blue triangles) shows only the transition corresponding to WAF (G_cC_b) order. If the low

temperature WFM spin order F_a phase had been coupled to the WAF spin order phase C_b, the FC procedure would have revealed an additional magnetization below $T_{C1} = 19$ K, but this was not the case. Finally, a simple FC down to 5 K in 1 kOe yielded the TRM curve (Figure 8, black squares) representing the sum of both transitions.

Finally, the question remains of why the transition from a collinear AF bulk phase G_c to the WAF (in theory) G_cC_b phase, $G_c \Rightarrow G_cC_b$, causes an observable response in the uncompensated magnetization (Figures 6b and 8), when the G_cC_b state is nominally antiferromagnetic. We suggest that growth-induced defects are responsible for the distorted spin compensation when the spin phase is WAF G_cC_b. We note that in antiferromagnets with structural disorder, the TRM response usually has a WFM signal due to uncompensated moments at domain boundaries or piezomagnetism.[47–49] It is also not uncommon for materials with collinear AF spin order in the bulk form to show WFM uncompensated moments when grown in thin film form.[50–55] Here we observe a similar situation, though more complicated: growth defects distort the absolute spin compensation in the WAF phase G_cC_b, that can cause the exchange interaction strength to fluctuate slightly throughout the film volume. Therefore, a weak uncompensated moment is observed (≈ 0.01 μ_B per magnetic ion, compared to the WAF moment ≈ 0.1 μ_B in Table 1).

4 Conclusions

$BaCoF_4$ thin films were synthesized for the first time. The films were grown with the single out-of-plane orientation of the b-axis, and with three in-plane domains with their polar c-axes rotated at 120° with respect to each other. Due to the lattice mismatch with the (0001) Al_2O_3 substrates, the corresponding out-of-plane b-axis and in-plane a-axis lattice parameters were smaller than in the bulk, while the in-plane c-lattice parameter, representing the polar axis, was larger than in the bulk.

FE field switching was observed in $BaCoF_4$ thin films at both room temperature (using

PFM) and at low temperatures (using remanent hysteresis loops). The PFM data were consistent with the three in-plane structural domains with the polar c-axis oriented at 120° with respect to each other, observed using XRD. The PFM data also revealed that different regions had different fields at which their polarizations could be reversed.

A broad peak in the magnetic susceptibility was observed close to the Nel temperature of the bulk $BaCoF_4$ compound, however additional WFM responses were found at temperatures below $T = 19$ K and 41 K. The maximum measured WFM moment was 0.03 μ_B per formula unit. Strong magnetic fields up to 30 kOe were required to saturate WFM loops at $T = 5$ K, thus demonstrating the AF nature of the magnetic interactions.

First-principles calculations were used to study the magnetic and FE properties of the $BaCoF_4$ as a function of the ac-plane epitaxial strain. The calculations indicated the existence of a non-linear polarization-strain coupling, suggesting a second-order piezoelectric response. An enhancement of the polarization was observed for non-zero strain values. For the value of epitaxial strain corresponding to the real thin films, a non-collinear ground state was found, with two additional WAF and WFM canted orders along the b- and a-axes, respectively. The sequence of magnetic transitions, $G_cC_bF_a \Rightarrow G_cC_b \Rightarrow G_c$, was predicted to take place with increasing temperature, starting from the magnetic ground state $G_cC_bF_a$. This result was consistent with the magnetic transitions found in the experimental TRM data.

Acknowledgement

This work was supported by the DMREF program of the US National Science Foundation (grant# DMR-1434897) and the WVU Shared Research Facilities.

References

(1) Cohen, R. E. Origin of Ferroelectricity in Perovskite Oxides. *Nature* **1992**, *358*, 136–138.

(2) Hill, N. A. Why Are There So Few Magnetic Ferroelectrics? *J. Phys. Chem. B* **2000**, *104*, 6694–6709.

(3) Scott, J. F.; Blinc, R. Multiferroic Magnetoelectric Fluorides: Why Are There So Many Magnetic Ferroelectrics? *J. Phys. C: Condens. Mat.* **2011**, *23*, 113202.

(4) Ederer, C.; Spaldin, N. A. Electric-Field-Switchable Magnets: The Case of $BaNiF_4$. *Phys. Rev. B* **2006**, *74*, 020401.

(5) Ederer, C.; Spaldin, N. A. Origin of Ferroelectricity in the Multiferroic Barium Fluorides $BaMF_4$: A First Principles Study. *Phys. Rev. B* **2006**, *74*, 024102.

(6) DiDomenico Jr, M.; Eibschütz, M.; Guggenheim, H. J.; Camlibel, I. Dielectric Behavior of Ferroelectric $BaMF_4$ Above Room Temperature. *Solid. St. Commun.* **1969**, *7*, 1119–1122.

(7) Keve, E. T.; Abrahams, S. C.; Bernstein, J. I. Ferroelectric Paraelastic Paramagnetic Barium Cobalt Fluoride, $BaCoF_4$, Crystal Structure. *J. Phys. Chem.* **1970**, *53*, 3279–3287.

(8) Cox, D. E.; Eibschütz, M.; Guggenheim, H. J.; Holmes, L. Neutron Diffraction Study of Magnetic Structure of $BaNiF_4$. *J. Appl. Phys.* **1970**, *41*, 943–945.

(9) Eibschütz, M.; Guggenheim, H. J. Antiferromagnetic-Piezoelectric Crystals: $BaMe_4$ (M = Mn, Fe, Co and Ni). *Solid. St. Commun.* **1968**, *6*, 737–739.

(10) Eibschütz, M.; Guggenheim, H. J.; Wemple, S. H.; Camlibel, I.; DiDomenico, M. Ferroelectricity in $BaM^{2+}F_4$. *Phys. Lett. A* **1969**, *A 29*, 409–410.

(11) Eibschütz, M.; Holmes, L.; Guggenheim, H. J.; Cox, D. E. Magnetic Structure of the Two-Dimensional Antiferromagnet $BaCoF_4$. *Phys. Rev. B* **1972**, *6*, 2677–2683.

(12) Glass, A. M.; Lines, M. E.; Eibschütz, M.; Hsu, F. S. L.; Guggenheim, H. J. Observation of Anomalous Pyroelectric Behavior in $BaNiF_4$ Due to Cooperative Magnetic Singularity. *Commun. Phys.* **1977**, *2*, 103–107.

(13) Scott, J. F. Mechanisms of Dielectric Anomalies in $BaMnF_4$. *Phys. Rev. B* **1977**, *16*, 2329–2331.

(14) Scott, J. F. Phase-Transitions in $BaMnF_4$. *Rep. Prog. Phys.* **1979**, *42*, 1055–1084.

(15) Kleemann, W.; Schafer, F. J.; Nouet, J. Linear Magnetic Birefringence and Double-Excitonic Transitions of the Two-Dimensional Antiferromagnet $BaNiF_4$. *J. Phys. C: Solid State Phys.* **1981**, *14*, 4447–4461.

(16) von Schnering, H. G.; Bleckmann, P. Ternary Fluoride ABF_4 of a New Structural Type. *Naturwissenschaften* **1968**, *55*, 342–343.

(17) Cordrey, K. J.; Stanczyk, M.; Dixon, C. A. L.; Knight, K. S.; Gardner, J.; Morrison, F. D.; Lightfoot, P. Structural and Dielectric Studies of the Phase Behaviour of the Topological Ferroelectric $La_{1-x}Nd_xTaO_4$. *Dalton Trans.* **2015**, *44*, 10673–10680.

(18) Stokes, H. T.; Hatch, D. M. FINDSYM: Program for Identifying the Space-Group Symmetry of a Crystal. *J. Appl. Cryst.* **2005**, *38*, 237–238.

(19) Al'shin, B.; Astrov, D.; Tishchenko, A.; Petrov, S. Magnetoelectric Effect in $BaCoF_4$. *Sov. Phys. - JETP Lett.* **1970**, *12*, 142–144.

(20) Al'shin, B.; Astrov, D.; Tishchenko, A.; Petrov, S. Magnetoelectric Effect in $BaCoF_4$. *ZhETF Pis. Red.* **1970**, *12*, 206–209.

(21) Fox, D. L.; Tilley, D. R.; Scott, J. F.; Guggenheim, H. J. Magnetoelectric Phenomena in $BaMnF_4$ and $BaMn_{0.99}Co_{0.01}F_4$. *Phys. Rev. B* **1980**, *21*, 2926–2936.

(22) Tilley, D. R.; Scott, J. F. Frequency Dependence of Magnetoelectric Phenomena in $BaMnF_4$. *Phys. Rev. B* **1982**, *25*, 3251–3260.

(23) Quilichini, M.; Ryan, J.; Scott, J. Light Scattering From Soft Modes in Ferroelectric $BaZnF_4$ and $BaMgF_4$. *Solid St. Commun.* **1975**, *16*, 471–475.

(24) Scott, J.; Tilley, D. Magneto-Electric Anomalies in $BaMnF_4$. *Ferroelectrics* **1994**, *161*, 235–243.

(25) Ghosez, P.; Triscone, J.-M. Multiferroics: Coupling of the Three Lattice Instabilities. *Nat. Mater.* **2011**, *10*, 269–270.

(26) Benedek, N. A.; Fennie, C. J. Hybrid Improper Ferroelectricity: A Mechanism for Controllable Polarization-Magnetization Coupling. *Phys. Rev. Lett.* **2011**, *106*, 107204.

(27) Kresse, G.; Furthmüller, J. Efficient Iterative Schemes for Ab-Initio Total-Energy Calculations Using a Plane-Wave Basis Set. *Phys. Rev. B* **1996**, *54*, 11169–11186.

(28) Kresse, G.; Joubert, D. From Ultrasoft Pseudopotentials to the Projector Augmented-Wave Method. *Phys. Rev. B* **1999**, *59*, 1758–1775.

(29) Blöchl, P. E. Projector Augmented-Wave Method. *Phys. Rev. B* **1994**, *50*, 17953–17979.

(30) Perdew, J. P.; Ruzsinszky, A.; Csonka, G. I.; Vydrov, O. A.; Scuseria, G. E.; Constantin, L. A.; Zhou, X.; Burke, K. Restoring the Density-Gradient Expansion for Exchange in Solids and Surfaces. *Phys. Rev. Lett.* **2008**, *100*, 136406.

(31) Liechtenstein, A. I.; Anisimov, V. I.; Zaanen, J. Density-Functional Theory and Strong Interactions: Orbital Ordering in Mott-Hubbard Insulators. *Phys. Rev. B* **1995**, *52*, R5467–R5470.

(32) Hobbs, D.; Kresse, G.; Hafner, J. Fully Unconstrained Noncollinear Magnetism Within the Projector Augmented-Wave Method. *Phys. Rev. B* **2000**, *62*, 11556–11570.

(33) King-Smith, R. D.; Vanderbilt, D. Theory of Polarization of Crystalline Solids. *Phys. Rev. B* **1993**, *47*, 1651–1654.

(34) Vanderbilt, D.; King-Smith, R. D. Electric Polarization as a Bulk Quantity and Its Relation to Surface Charge. *Phys. Rev. B* **1993**, *48*, 4442–4455.

(35) Resta, R. Macroscopic Polarization in Crystalline Dielectrics: the Geometric Phase Approach. *Rev. Mod. Phys.* **1994**, *66*, 899–915.

(36) Villora, E. G.; Shimamura, K.; Jing, F. L.; Medvedev, A.; Takekawa, S.; Kitamura, K. Ferroelectric and Optical Properties of Single Crystal $BaZnF_4$. *Appl. Phys. Lett.* **2007**, *90*, 192909.

(37) Dawber, M.; Rabe, K. M.; Scott, J. F. Physics of Thin-Film Ferroelectric Oxides. *Rev. Mod. Phys.* **2005**, *77*, 1083–1130.

(38) Güthner, P.; Dransfeld, K. Local Poling of Ferroelectric Polymers by Scanning Force Microscopy. *Appl. Phys. Lett.* **1992**, *61*, 1137–1139.

(39) Kalinin, S. V.; Rodriguez, B. J.; Jesse, S.; Shin, J.; Baddorf, A. P.; Gupta, P.; Jain, H.; Williams, D. B.; Gruverman, A. Vector Piezoresponse Force Microscopy. *Microsc. Microanal.* **2006**, *12*, 206–220.

(40) Xu, R.; Liu, S.; Grinberg, I.; Karthik, J.; Damodaran, A. R.; Rappe, A. M.; Martin, L. W. Ferroelectric Polarization Reversal via Successive Ferroelastic Transitions. *Nat. Mater.* **2015**, *14*, 79–86.

(41) Balke, N.; Choudhury, S.; Jesse, S.; M., H.; Chu, Y. H.; Baddorf, A. P.; Chen, L. Q.; Ramesh, R.; Kalinin, S. V. Deterministic Control of Ferroelastic Switching in Multiferroic Materials. *Nat. Nanotechnol.* **2009**, *4*, 868–875.

(42) Zhao, T.; Scholl, A.; Zavaliche, F.; Lee, K.; Barry, M.; Doran, A.; Cruz, M. P.; Chu, Y. H.; Ederer, C.; Spaldin, N. A.; Das, R. R.; Kim, D. M.; Baek, S. H.; Eom, C. B.;

Ramesh, R. Electrical Control of Antiferromagnetic Domains in Multiferroic $BiFeO_3$ Films at Room Temperature. *Nat. Mater.* **2006**, *5*, 823–829.

(43) Scola, J.; Boullay, P.; Noun, W.; Popova, E.; Dumont, Y.; Fouchet, A.; Keller, N. Microstructure and Self-Exchange Coupling in a $YFeO_3$ film. *J. Appl. Phys.* **2011**, *110*, 043928.

(44) Ederer, C.; Spaldin, N. A. Effect of Epitaxial Strain on the Spontaneous Polarization of Thin Film Ferroelectrics. *Phys. Rev. Lett.* **2005**, *95*, 257601.

(45) Bester, G.; Wu, X.; Vanderbilt, D.; Zunger, A. Importance of Second-Order Piezoelectric Effects in Zinc-Blende Semiconductors. *Phys. Rev. Lett.* **2006**, *96*, 187602.

(46) García-Castro, A. C.; Romero, A. H.; Bousquet, E. Noncollinear Magnetism in Post-Perovskites From First Principles: Comparison Between $CaRhO_3$ and $NaNiF_3$. *Phys. Status Solidi (b)* **2015**, *252*, 689–694.

(47) Han, S. J.; Belanger, D. P.; Kleemann, W.; Nowak, U. Relaxation of the Excess Magnetization of Random-Field-Induced Metastable Domains in $Fe_{0.47}Zn_{0.53}F_2$. *Phys. Rev. B* **1992**, *45*, 9728–9735.

(48) Lederman, M.; Hammann, J.; Orbach, R. Net Spontaneous Magnetisation in the Dilute Ising Antiferromagnet $Fe_{.46}Zn_{.54}F_2$. *Phys. B* **1990**, *165166*, 179–180.

(49) Pérez, F. A.; Borisov, P.; Johnson, T. A.; Stanescu, T. D.; Trappen, R.; Holcomb, M. B.; Lederman, D.; Fitzsimmons, M. R.; Aczel, A. A.; Hong, T. Phase Diagram of a Three-Dimensional Antiferromagnet with Random Magnetic Anisotropy. *Phys. Rev. Lett.* **2015**, *114*, 097201.

(50) Munbodh, K.; Cheon, M.; Lederman, D.; Fitzsimmons, M. R.; Dilley, N. R. Interfacial Coupling Between Ferromagnets and Random and Dilute Antiferromagnets. *Phys. Rev. B* **2011**, *84*, 214434.

(51) Ohldag, H.; Shi, H.; Arenholz, E.; Stöhr, J.; Lederman, D. Parallel Versus Antiparallel Interfacial Coupling in Exchange Biased Co/FeF_2. *Phys. Rev. Lett.* **2006**, *96*, 027203.

(52) Brück, S.; Schtz, G.; Goering, E.; Ji, X.; Krishnan, K. M. Uncompensated Moments in the MnPd/Fe Exchange Bias System. *Phys. Rev. Lett.* **2008**, *101*, 126402.

(53) Arenholz, E.; Liu, K.; Li, Z.; Schuller, I. K. Magnetization Reversal of Uncompensated Fe Moments in Exchange Biased Ni/FeF_2 Bilayers. *Appl. Phys. Lett.* **2006**, *88*, 072503.

(54) Roy, S.; Fitzsimmons, M. R.; Park, S.; Dorn, M.; Petracic, O.; Roshchin, I. V.; Li, Z.-P.; Batlle, X.; Morales, R.; Misra, A.; Zhang, X.; Chesnel, K.; Kortright, J. B.; Sinha, S. K.; Schuller, I. K. Depth Profile of Uncompensated Spins in an Exchange Bias System. *Phys. Rev. Lett.* **2005**, *95*, 047201.

(55) Zhou, X.; Ma, L.; Shi, Z.; Fan, W. J.; Evans, R. F. L.; Zheng, J.-G.; Chantrell, R. W.; Mangin, S.; Zhang, H. W.; Zhou, S. M. Mapping Motion of Antiferromagnetic Interfacial Uncompensated Magnetic Moment in Exchange-Biased Bilayers. *Sci. Rep.* **2015**, *5*, 9183.

Graphical TOC Entry

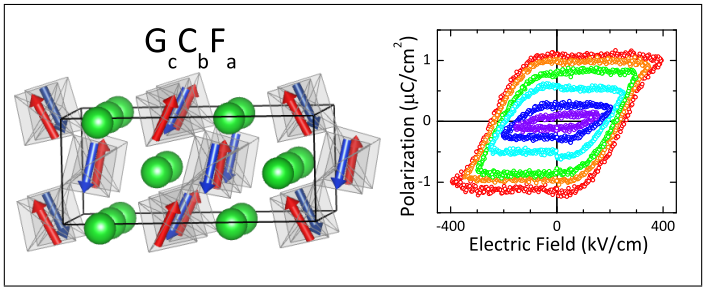

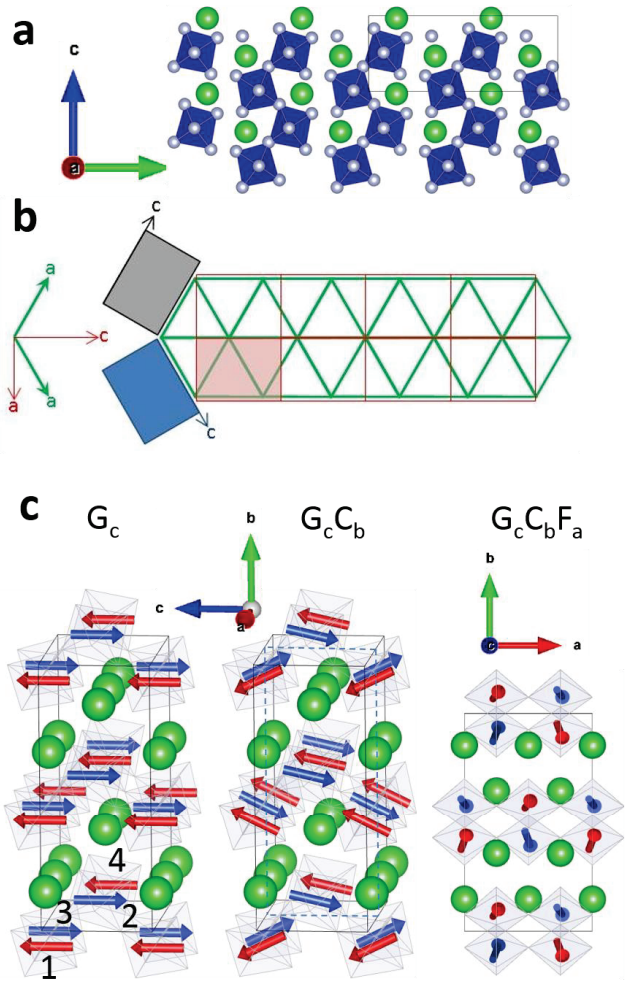

Figure 1: **Crystal and spin structure of $BaCoF_4$.** a: Projection of the $BaCoF_4$ structure on the $b-c$ plane. Ba and F atoms are large green and small gray spheres, respectively. CoF_6 octahedra are drawn in blue. The orthorhombic unit cell projection is drawn by a thin gray line. b: Illustration of the in-plane epitaxial relationship between the c-cut Al_2O_3 substrate (hexagonal unit cell, green lines and axis) and (010) $BaCoF_4$ thin films (orthorhombic unit cell, red lines and axis).Three structural domains are indicated by the light red, blue and gray areas c: From the left to the right: AF spin structures in $BaCoF_4$. The structure on the left represents bulk collinear structure (G_c) with spins along the c-axis. The one at the center includes additional weak AF canting (C_b) with the canted AF vector along b-axis. Spin canting is magnified with respect to the actual values for illustrative purposes. Note the alternation of the absolute spin canting angle if followed along the c-axis. The structure on the right has an additional WFM canting (F_a) with the magnetization along the a-axis and represents the ground state as calculated for the experimental anisotropic strain values applied to the $BaCoF_4$ unit cell.

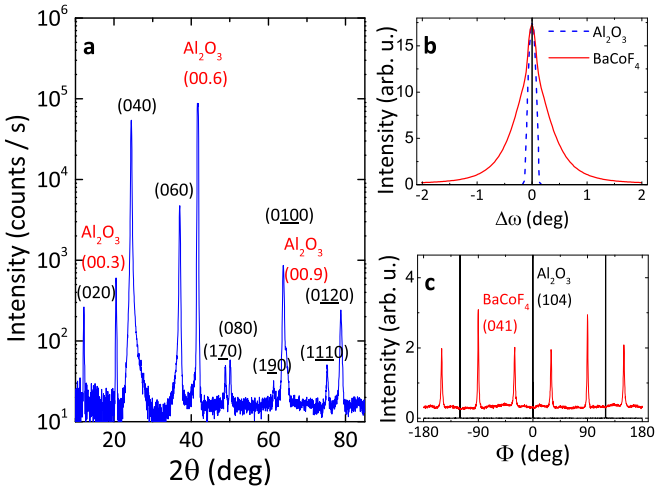

Figure 2: **X-ray diffraction structural characterization.** a: XRD $\theta - 2\theta$ scan from a $BaCoF_4$ thin film grown on an Al_2O_3 (0001) substrate. b: Rocking curves taken about the Al_2O_3 (0006) (blue dotted curve), the $BaCoF_4$ (040) (red solid curve) reflections. c: Φ-scans of (041) and $(10\bar{1}4)$ peaks for the $BaCoF_4$ film (red curve) and Al_2O_3 substrate (black curve).

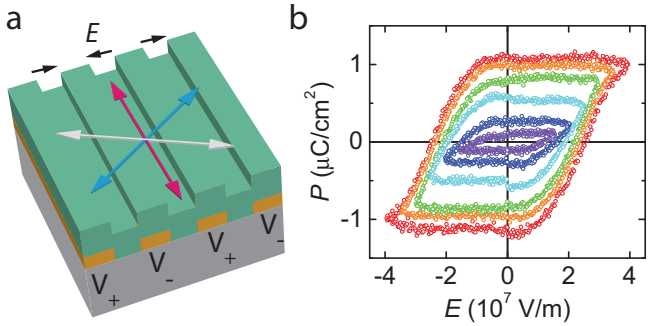

Figure 3: **Ferroelectric hysteresis measurements.** a: Interdigitated electrodes were deposited on the Al_2O_3 substrate and covered with the film. The electric field direction was aligned perpendicular to one of the structural twin domains (polar c-axis noted as red arrow) and at 30° with respect to the other two (blue and grey). Electrodes are separated by 2.5 μm. b: Remanent ferroelectric polarization vs. applied electric in-plane field measured on a $BaCoF_4$ thin film at $T = 14 \pm 2$ K.

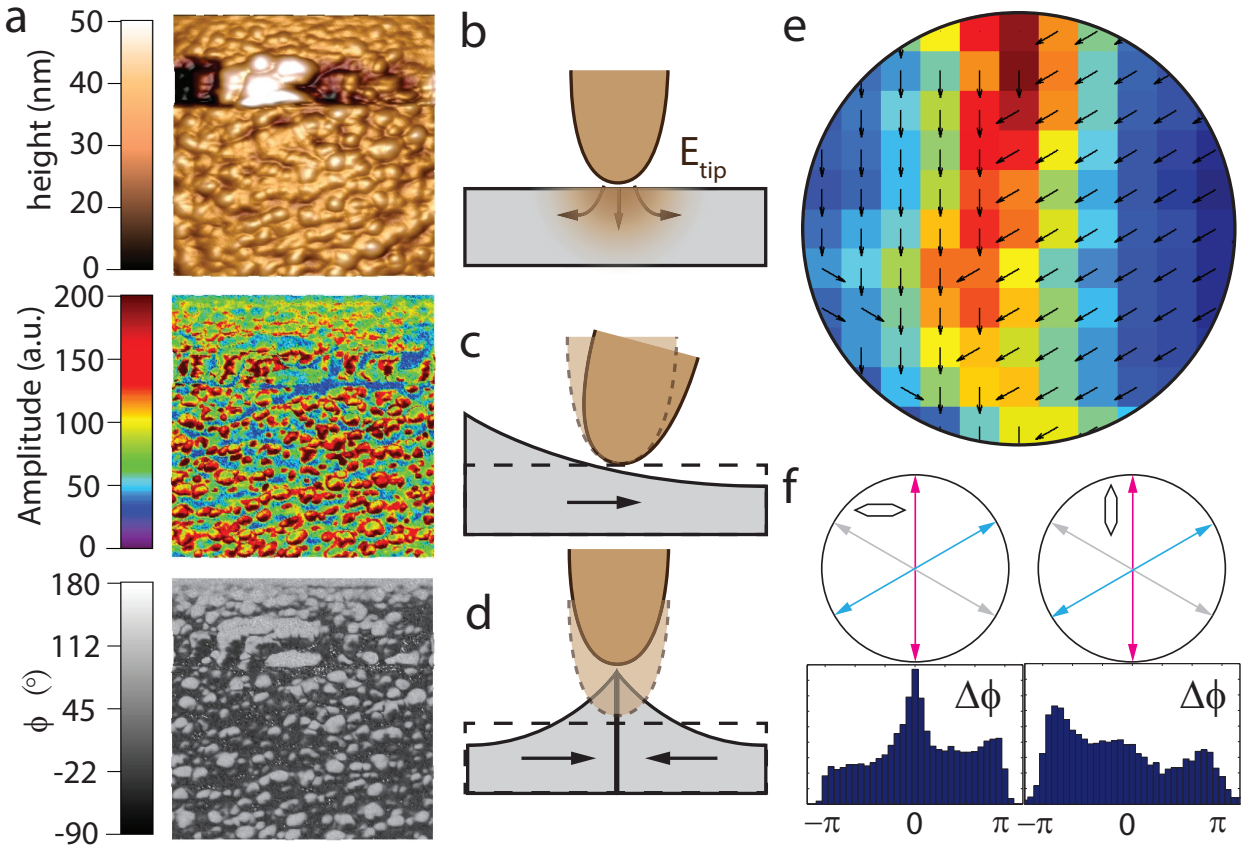

Figure 4: **Piezoresponse force microscopy (PFM) results.** a: Typical images of topography (top), PFM amplitude (middle) and PFM phase (bottom) in a 1.5 μm $\times$ 1.5 μm area. b: Schematic of tip field during PFM measurements. c: Surface deformation when tip scans the middle of an in-plane polarized domain. d: Surface deformation when tip scans over the boundary region between two domains with head-to-head polarizations. e: Vector plot of local domain polarizations overlaid on top of the PFM amplitude intensity image. This information is extracted from a collection of four PFM measurements with different cantilever orientations. f: Histograms of PFM phase change $\Delta\phi$ after 180° sample rotation for two orthogonal cantilever orientations noted by a small hexagon. When the cantilever is perpendicular to the polar c-axis in one of the structural twin domains (red), a large distribution at $\Delta\phi = 0$ is observed.

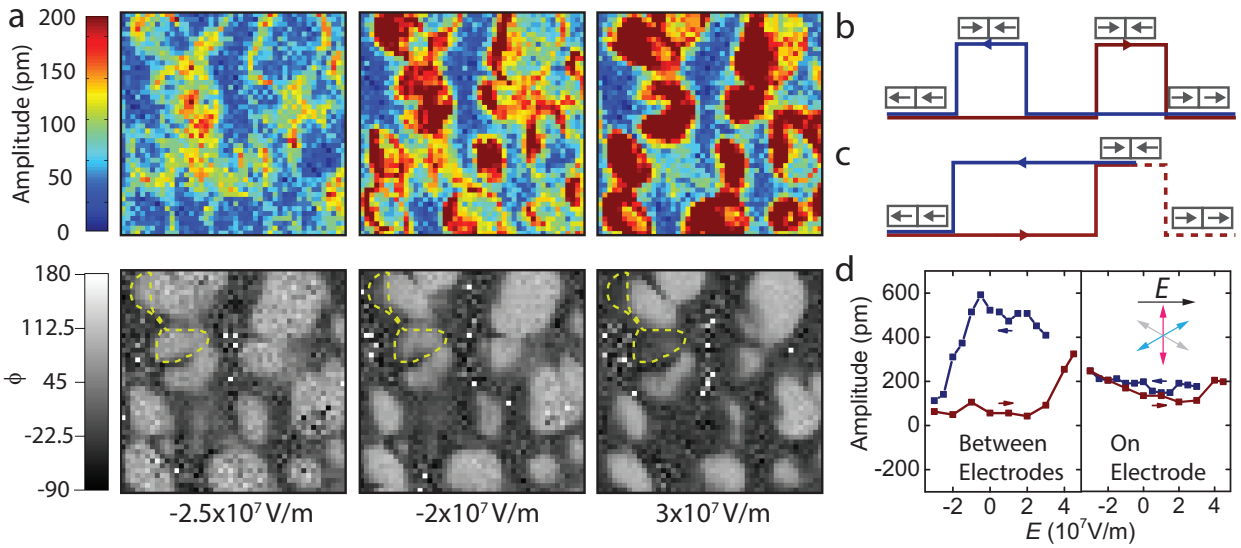

Figure 5: **Ferroelectric switching at room temperature.** a: PFM amplitude and phase measured in a 175 nm $\times$ 175 nm area after the application of different in-plane electric fields for 30 s. Areas enclosed by yellow dashed curves indicate regions switched by electric field. b, c: Illustration of idealized PFM amplitude changes at the boundary between two domains during electric field sweeps shown in (d). Red and blue lines correspond to decreasing and increasing field values, respectively. b: Maximum amplitude is expected when the two adjacent domains have opposite polarizations, noted by arrows in boxes. c: When the range of electric field is limited and some domains remain unswitched, the result shows a different PFM amplitude evolution. d: Experimental evolution of the PFM amplitude at two boundary spots when cycling the in-plane field. Left: between electrodes where in-plane field is properly applied; Right: on top of an electrode where no in-plane field is applied. Within the applied field range some domains did not switch, producing a PFM amplitude hysteresis, which highly resembled (c).

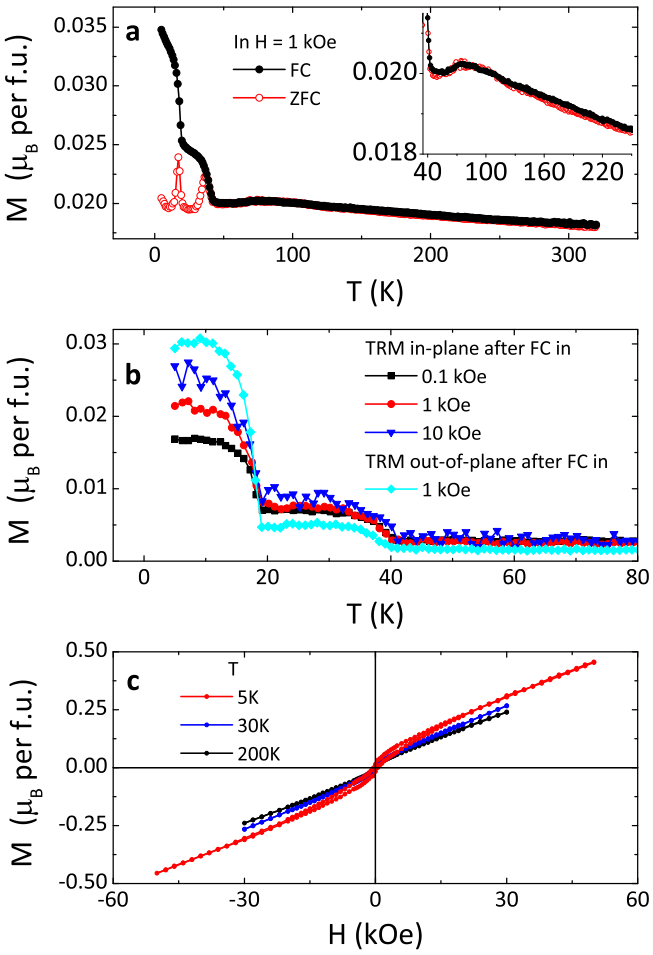

Figure 6: **Magnetic properties.** a: ZFC and FC magnetization M vs. temperature T for a $BaCoF_4$ film measured in $H = 1$ kOe applied in-plane. Inset provides magnified views of data showing the broad transition near $T = 80$ K. b: TRM vs. T after field-cooling in different magnetic fields. c: Magnetic hysteresis loops measured at different temperatures.

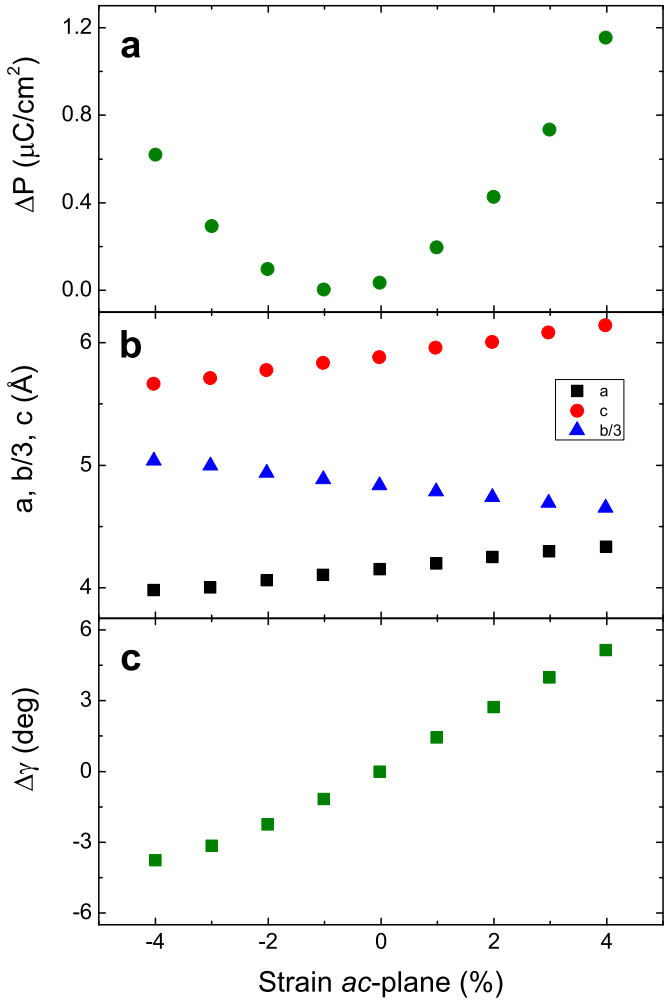

Figure 7: **Theoretical calculations of the epitaxial strain dependence of ferroelectric and structural properties.** a: Calculated polarization change along the c-axis as function of isotropic strain in the ac plane for $BaCoF_4$. b: Evolution of the lattice parameter as a function of strain. As the biaxial strain in the ac-plane increases, the b lattice parameter decreases. c: Deviation from the bulk Co-F-Co angle value along the a-axis as a function of the ac-plane epitaxial isotropic strain.

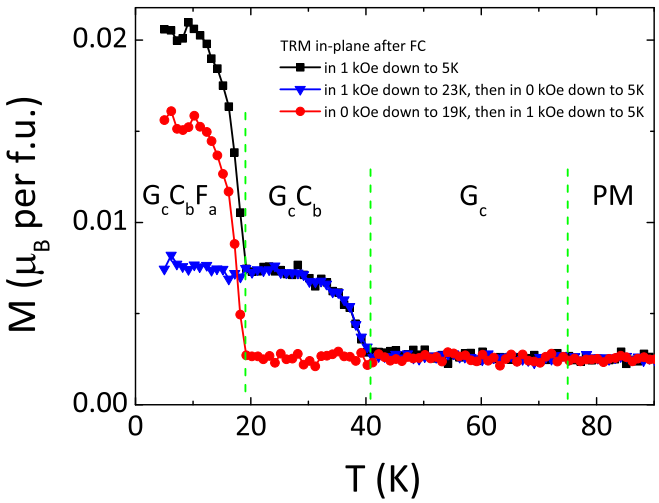

Figure 8: **Experimental illustration of low temperature magnetic phases.** TRM magnetization M data for a $BaCoF_4$ film measured under different protocols that correspond to the magnetic phases indicated in the graph. PM denotes the paramagnetic phase.